Ozone and carbon monoxide at the Ushuaia GAW-WMO global station

J.A. Adame, M. Cupeiro, M. Yela, E. Cuevas, G. Carbajal

PII: S0169-8095(18)30790-7
DOI: doi:10.1016/j.atmosres.2018.10.015
Reference: ATMOS 4396

To appear in: *Atmospheric Research*

Received date: 21 June 2018
Revised date: 22 October 2018
Accepted date: 24 October 2018

Please cite this article as: J.A. Adame, M. Cupeiro, M. Yela, E. Cuevas, G. Carbajal , Ozone and carbon monoxide at the Ushuaia GAW-WMO global station. Atmos (2018), doi:10.1016/j.atmosres.2018.10.015

Ozone and carbon monoxide at the Ushuaia GAW-WMO global station

Adame, J.A.[a,*], Cupeiro, M.[b], Yela, M.[a], Cuevas, E.[c], Carbajal, G.[d,e]

[a]Atmospheric Research and Instrumentation Branch, National Institute for Aerospace Technology (INTA), Torrejón de Ardoz, Madrid, Spain.

[b]Ushuaia GAW Station, National Meteorological Service (SMN), Ushuaia, Argentina

[c]Izaña Atmospheric Research Center, State Meteorological Agency of Spain (AEMET), Santa Cruz de Tenerife, Spain

[d]National Meteorological Service (SMN), Atmospheric Watch and Geophysical (GIDyC – VAYGEO), Buenos Aires, Argentina.

[e]Pontificia Universidad Católica Argentina, PEPACG, Facultad de Ingeniería y Ciencias Agrarias, Buenos Aires, Argentina.

[*]Corresponding author E-mail address: adamecj@inta.es (J.A. Adame)

Abstract

Five years (2010-2014) of hourly surface measurements of ozone (O_3) and carbon monoxide (CO) at the GAW-WMO station in Ushuaia (Argentina) were analysed and characterised. A meteorological study of the region was carried out using in situ observations and meteorological fields from the ECMWF (European Centre for Medium-Range Weather Forecast) global meteorological model. Atmospheric transport was investigated with the air mass trajectories computed with HYSPLIT (Hybrid Single Particle Lagrangian Integrated Trajectory) model using ERA-Interim meteorological fields. Airflows primarily arise from the W-SW (South Pacific Ocean) which are associated with an almost permanent low pressure system. Collected winds from the South (Antarctic Peninsula and Weddell Sea), polar easterlies, occur less frequently. The hourly averages of O_3 and CO were 20±7 ppb and 71±45 ppb, respectively, typical values in remote environments. A clear seasonal pattern was obtained for O_3, with a monthly peak in winter of 25 ppb and minimum in summer of 12 ppb. Similar behaviour was found for CO, with 93 and 48 ppb maximum and minimum values, respectively. Both species show a weak daily cycle with an amplitude of 2-4 ppb for O_3 and 13-20 ppb for CO. Peaks in O_3 and CO in the cold season could be associated with low photochemical activity, fewer destructive processes and transport of these species from the South Pacific. O_3 vertical behaviour was analysed using 139 O_3 soundings at Ushuaia in the period studied. The seasonal patterns and levels of the O_3 profiles from the surface up to 5 km are similar to measurements on surface and thus it can be assumed that the O_3 measured on the surface could be representative of the low-mid troposphere. To investigate the spatial distribution of O_3 and CO in this region and the spatial representativeness of the Ushuaia measurements, daily observations from the AIRS (Atmospheric Infrared Sounder) instrument on board the AQUA satellite were used. The results obtained show that the O_3 levels in Ushuaia could be representative of a wide region in the Pacific South and that the CO levels are representative of a continental region around the observatory.

Highlights

- The levels, seasonal and daily variations of O_3 and CO at the Ushuaia GAW are analysed.
- The meteorology in this region is governed by westerly flows.
- O_3 and CO reached a maximum in winter and a minimum in summer.
- O_3 soundings and AIRS satellite observations were used.

- O_3 measurements are representative of the MBL in the South Pacific and CO of a continental local area.

Keywords: Surface ozone; carbon monoxide; Ushuaia GAW-WMO global station; AIRS instrument.

1. Introduction

Ozone (O_3) and carbon monoxide (CO) on the Earth's surface have a substantial impact on atmospheric chemistry, air quality and the climate. They are two key species in the photochemical system of the troposphere. The atmospheric chemistry of O_3 is an important context to understand the connections between air quality and climate change because it is linked to many indirect effects (Von Schneidemesser et al., 2015). CO contributes to positive radiative forcing (warming) through its role in O_3 production and through an increase in methane persistence.

O_3 undergoes complex atmospheric formation and destruction chemistry that causes O_3 concentrations to vary widely on geographical and temporal scales (Schnell et al., 2015; Hardacre et al., 2015; Verma et al., 2017). Tropospheric O_3 controls the oxidizing capacity of the atmosphere by photolysis and reactions with water vapor (H_2O) that form OH radicals, and as a greenhouse gas (Logan et al., 1981). O_3 is produced in the troposphere through photochemical oxidation of methane (CH_4), CO, and non-methane volatile organic compounds (NMVOCs) in the presence of nitrogen oxides (NO_x). Ozone is formed, typically referred to as NOx-sensitive and VOC-sensitive in two chemical regimes. The regimes are identified according to the VOC/NOx ratios, VOC reactivity, biogenic emissions, photochemical ageing and meteorological conditions. Moreover, the type of regime is closely associated with sources (produced by photolysis of O_3, HCHO, and other intermediate organics) and sinks of odd hydrogen radicals (Von Schneidemesser et al., 2015).

Clean air environments such as the MBL (Marine Boundary Layer) with low NO_x are NOx-sensitive, i.e., net ozone sinks (He et al., 2016). Ozone in the MBL is mainly destroyed by photo dissociation ($O_3+h\nu \rightarrow O_2+O(^1D)$), subsequent reaction of $O(^1D)$ with water vapour ($O(^1D) + H_2O \rightarrow 2OH$) and production of OH radical or is attacked by OH and HO_2 radicals ($OH+O_3 \rightarrow O_2+HO_2$ and $HO_2+O_3 \rightarrow OH+2O_2$) that are formed photochemically from solar radiation. In the absence of NO_x, which would favour ozone formation, the net balance is ozone destruction.

O_3 causes harmful effects on human health, animals and vegetation on earth (Lefohn et al., 2017) and has a significant contribution as a greenhouse gas because its long-term concentration changes have increased the radiative forcing of climate (IPCC, 2014).

CO is primarily emitted from combustion processes but is also formed in substantial amounts from the oxidation of methane (CH_4) and volatile organic compounds (VOCs). The primary sink of CO is oxidation by the hydroxyl radical (OH). CO is a major O_3 precursor and has a strong impact on its oxidizing capacity and thus indirectly impacts the concentration of the climate gas CH_4. CO controls the concentrations and distributions of atmospheric oxidants such as O_3, hydroperoxy (HO_2) and hydroxyl (OH) radicals (Seinfeld and Pandis, 1998). An increase in CO is expected to decrease OH and to increase the lifetime and abundance of these gases. CO has a lifetime of weeks to months and thus is an ideal tracer of transport processes. CO originating in polluted areas often produces significant enhancements over background values at distant sites.

High-latitude regions (Antarctica and surroundings) are of interest in investigating O_3 and CO behaviour for several reasons: i) anthropogenic sources and sinks are scarce due to low human population density and the general absence of industries; ii) O_3 and CO in these environments are determined by natural processes, synoptic transport and downward transport from upper layers (Ali et al., 2017) and it is recognized as a climate-sensitive hotspot region (IPCC, 2014). Consequently, O_3 data from these high latitudes are of interest for assessing O_3 background levels and trends at hemispheric scales (Legrand et al., 2009).

The World Meteorological Organization (WMO) Global Atmosphere Watch (GAW) Programme comprises a large worldwide observation network and the spatial representativeness of the measurements at each observatory is of interest (Sofen et al., 2016) to use the information as input in global transport and other models. In addition, the data collected at GAW stations such as the Ushuaia station is useful for conducting global studies (Tarasova et al., 2007; Boylan et al., 2015; Cooper et al., 2014; Parrish et al., 2016). However, use of these databases in research to improve the knowledge of physical and chemical atmospheric processes of these regions is lacking.

This work examines a five-year (2010-2014) record of O_3 and CO measurements at the Ushuaia GAW station, to investigate the annual, monthly and daily evolution of these species and discover their spatial (horizontal and vertical) representativeness and origins. To achieve this, a meteorological analysis of the region was performed (section 3.1). The analysis of the values, seasonal and diurnal evolutions of O_3 and CO is shown in section 3.2. In section 3.3 the vertical and horizontal distribution is investigated using O_3 profiles and satellite observations. Finally, in last section the Discussion and Conclusions are presented.

2. Experimental conditions and methods

2.1. Measurement site

The Ushuaia observatory (54° 50' S - 68° 18' W) is part of the GAW programme and is in the southwest Ushuaia Peninsula, southern Isla Grande de Tierra del Fuego, in a marine sub-Antarctic environment. It is approximately 5 km away from the city of Ushuaia, which has 75000 inhabitants. The observatory is a few metres from a coastal cliff, 17 m above sea level (asl). The Martial mountains of the Andes range are to the North, East and West and do not exceed 1400 m asl, the Beagle channel and Navarino and Hoste islands are to the South. Grasses and small shrubs are the typical vegetation in the zone, with sub-Antarctic (Magallanic) forest (Nothofagus) prevailing. The main atmospheric emissions sources have origins in fossil fuels burned for domestic heating, low vehicular traffic and power generation from cities on the island, Ushuaia, Rio Grande, and the city of Punta Arenas to the northwest. There are no significant industrial, agriculture or livestock activities in the area. In this region the summer covers December to February, autumn from March to May, winter from June to August and spring from September to November.

2.2. Instrumentation and data

O_3 was measured by UV absorption using a TEI 49C (Thermo Electron Corporation, Environmental Instruments). CO was measured by nondispersive IR absorption photometry (NDIR) using a HORIBA (APMA–360). In both cases, the data have a temporal resolution of one minute.

The air inlet system has an air intake 7 m above ground level over the observatory roof that consists of Teflon tubing flushed at 11 l min^{-1}. For O_3 and CO, an hour-long automatic zero check is performed daily. In addition, an automatic span calibration is performed daily for the CO instrument. Every four-months, a

manual calibration of span with three points (10, 50 and 100 ppb) for O_3 is performed and every six months a calibration with three points (200, 500 and 800 ppb) is performed for CO.

The O_3 analyzer is calibrated every year at the WMO-GAW Regional Calibration Centre for Surface Ozone (RCC-BsAs) in Buenos Aires (Argentina). The WMO/GAW World Calibration Centre WCC-EMPA for Surface Ozone, Carbon Monoxide, Methane and Carbon Dioxide, with instrumentation from the Swiss Federal Laboratories for Materials Science and Technology (EMPA), audits O_3 and CO instruments approximately every five years. For traceability of O_3 measurements, the standard scale of reference given by NIST SRP#15 and (for CO) the WMO-2000 is used. The zero values for O_3 and CO obtained in the daily calibrations are used to correct the data each minute and later are obtained the hourly values.

A Vaisala weather station is used to collect the pressure, temperature and relative humidity at 2m, and a Young instrument on a 10 m mast is used to measure the wind direction and speed. An Eppley pyranometer measures global solar radiation (integrated from 285 to 3000 nm). All the parameters are recorded with a 1 minute temporal resolution.

The measurements of O_3, CO and surface meteorology are available in the World Data Centre for Greenhouse Gases (WDCGG), specifically in the webpage: http://ds.data.jma.go.jp/gmd/wdcgg/.

Ozonesondes are launched routinely from the Ushuaia GAW station under a framework of collaboration between the National Meteorological Service (SMN) of Argentina, the State Meteorological Agency (AEMET) of Spain and the National Institute for Aerospace Technology (INTA) of Spain; there were approximately 150 O_3 soundings during the study period. Electro-chemical concentration cells (ECC) are used. The O_3 sensor consists of a coupled to a radiosonde from Vaisala that measures pressure, temperature, humidity and wind. The system is released with a TOTEX balloon (TX-1200) filled with helium. A TSC-1 ozonizer/test unit (Science Pump Corporation) was used for the preparation, calibration and ground check of ECC sondes according to World Meteorological Organization (WMO) recommendations (Smit et al., 2011). The ozone profiles are available in the webpage: https://woudc.org/home.php.

2.3. Meteorological and trajectory models and satellite observations

To investigate the synoptic conditions in this region, meteorological fields from the global ECMWF (European Centre for Medium Range Weather Forecasts) model were used, specifically the ERA-Interim (Dee et al., 2011) with spatial and temporal resolutions of 0.5^ox0.5^o (latitude x longitude) and 6 hours, respectively, and 26 vertical levels from the surface to 50 mb.

Air mass pathways were explored using the HYSPLIT (Hybrid Single-Particle Lagrangian Integrated Trajectory) model developed by the NOAA's Air Resources Laboratory (ARL) (Draxler et al., 2009). Three-dimensional kinematic daily back-trajectories were computed at 12:00 UTC, with a 120-hour pathway (5 days) at 500 m agl (above ground level) with an ending point at Ushuaia during the complete five-year period. The back trajectories were calculated using ERA-Interim meteorological fields that were converted to ARL, the standard format of the HYSPLIT model. A seasonal cluster analyzes have been applied to the back-trajectories, to identify atmospheric trajectory groups. In the HYSPLIT model, the clustering process is based in the spatial variance (SPVAR) and total spatial variance (TSV) (Stunder, 1996). Four clusters centres have been considered sufficient to capture the air masses variability in this region.

To investigate the spatial distribution on the surface, O_3 and CO satellite observations from the AIRS (Atmospheric Infrared Sounder) instrument on board of AQUA satellite were used (Aumann et al., 2003; Susskind et al., 2003; Nara et al., 2011; Lin et al., 2012). For this work, the AIRS Level 3 Daily Standard Physical Retrieval V006 (AIRX3STD) was used. The AIRS Level 3 daily data are gridded by 1°×1° (latitude × longitude) and the 1000 hPa level was selected for this study for comparison with the in situ surface measurements.

3. Results

3.1. Meteorological description

The synoptic conditions were studied using seasonal maps of the mean sea level pressure (MLP) using the ERA-Interim meteorological fields from the ECMWF global model. Figure 1 (a-b) illustrates a low-pressure system in the Pacific Ocean to the South and West of the Antarctica Peninsula. This is one of the low-pressure systems that surround the Antarctic continent and remains nearly constant throughout the year (Polian et al. 1986, Simmonds et al., 2003). This configuration generates westerly flows in an area from approximately 55° to 70° S latitude and 70° to 150° W longitude.

A seasonal cluster analysis has been carried out using four as an optimal number for the centre cluster. Fig. 1 (c-f) shows the seasonal pathways of cluster means back trajectories. The air masses arriving at Ushuaia can have its origin five days before at ~3500-5000 km away on the Southern Pacific, area between 60° and 80° N and 130° to 170° W, with a frequency between 45 and 77 % in summer and autumn respectively. With a shorter pathway, ~2500 km and origin in an area between 40° and 50° N and 80° to 100° W, have been obtained back-trajectories means, with a occurrence which vary between 8 and 28 % in spring and summer respectively. Finally, the air masses with the shortest route (~1000-1500 km) coming from a maritime zone located in the west of the Antarctica Peninsula (65°-70° N and 70°-90° W) with a frequency ranging between 11 and 34 % in autumn and spring. Therefore, the air masses that reach the Ushuaia region come from the West throughout the year and are oceanic and sub polar air from the Pacific South associated with the above mentioned low-pressure system. These results indicate that the surface air measured at this observatory could be representative of the MBL of the South Pacific Ocean.

The local weather conditions on the surface were analysed using the meteorological observations at the Ushuaia GAW station. Figure 2 presents the monthly evolutions for temperature, relative humidity, wind speed and global solar radiation and the seasonal diurnal variations for temperature and relative humidity.

Fig. 1.

The monthly evolution for global solar radiation shows minimum values in winter and peaks in summer, with an amplitude of 186 W m^{-2}. In summer months, the solar radiation oscillates from 170 to 204 W m^{-2}, decreases in autumn from 106 to 35 W m^{-2}, and reaches a minimum in the cold months of June and July, with monthly values of 17-23 W m^{-2}. In the Ushuaia region, there is no absolute darkness in wintertime. From August, the global solar radiation begins to increase, with values in spring from 100 to 190 W m^{-2}.

The temperature shows a clear monthly evolution, oscillating around ~9.0 °C in January and ~4.2 °C observed in the cold season, with a thermal amplitude of 5 °C. The diurnal variation is stable, with variations of 1-2 °C, and a maximum temperature at 18:00 UTC. With the exception of winter, with

temperatures ranging between 3 and 4 ^{o}C during the day, the temperature oscillates between 6 and 9 ^{o}C the remainder of the year. The relative humidity does not show a clear monthly variation, featured in coastal areas, minimum in October with 67% and maximum in June with 73%, during ten months the monthly values are ~70 %. As expected, a slight daily cycle was observed for the relative humidity, with a minimum at 18:00-19:00 UTC. The winter months present minimum values of 58-60 % and the remainder of the year has similar values of ~65-75 %.

Fig. 2.

The wind speed shows a seasonal variation with peaks in warm months (7.1±1.0 m s^{-1}) and low values in the cold season (4.2±0.4 m s^{-1}). The daily evolution of the wind speed (not shown in Fig. 2) presents three different patterns based on the time of year. In winter, no variations are observed, with values of 3.5 m s^{-1}. In autumn, a slight increase in the later hours that is more abrupt in spring/summer (peaks between 6 and 8 m s^{-1}) was observed, with an increase from 10:00 UTC and a decrease during the night.

Basically, the wind regime of this region is driven by the Beagle channel orography, the wind blows from two prevalent directions, west and east. In detail, the annual and seasonal wind roses present a clear main direction (not shown), with airflows blowing from WSW-W with a frequency greater than 35 % in winter and with a peak of 48 % in summer. In addition, these flows present the highest wind speeds. These westerly flows have origins in the isobaric configuration mentioned above. NW flows were also observed at lower frequencies and velocities, likely associated with a weak isobaric gradient. The calm conditions frequently occur in autumn (~10 %) and winter (~4 %) months.

3.2. O_3 and CO overview: annual, monthly and daily evolutions

Using the monthly values has been calculated the annual mean both for the O_3 and CO. For O3 the annual values vary between 19.8±4.6 ppb (in 2014) and 20.8±5.8 ppb (in 2012) with a mean of 20.3±5.2 ppb. In the case of CO, the values oscillate between 67.1±14.3 ppb (in 2010) and 75.0±19.3 ppb (in 2013) with a mean in the whole period of 71.5±16.6 ppb. Therefore, no variations year to year have been found in the five years of measures. These results could point out that there has not been a significant change in the weather or emission conditions which could affect O_3 and CO concentrations during this period.

In the five-year measurement period, hourly O_3 values showed a 95th percentile of 32.3 ppb and a 5th percentile of 8.4 ppb. The mean value was 20.3±7.6 ppb, with a median of 19.8 ppb, showing no large variations. The O_3 values registered at Ushuaia are similar to or slightly lower than those measured at other GAW stations of similar latitude. In Vingarzan (2004) were reported annual means ranging between 19 and 33 ppb in six remote sites around the world. For CO the 95th percentile was of 157 ppb and the 5th percentile of 40.8 ppb. The mean was 71.5±45.2 ppb, with a median of 60 ppb, and the CO variability is higher than that of O_3. The hourly minimum was 18 ppb (5th percentile of 40 ppb).

Figure 3 shows the monthly and diurnal variations for O_3 and CO. The monthly evolution of O_3 presents a clear variation, with a minimum in the summer months, 12-13 ppb in January and February, and peaks in winter of 25 ppb between June and August. Similar or lower values to the obtained in other works where O_3 was studied in this region (Nadzir et al., 2018). A low monthly deviation was observed, with values of 1-2 ppb, showing a low day-to-day variability. From January to June, a monthly increase of 2.5 ppb month^{-1} was observed, which could be associated with decreases in the temperature, solar radiation and dispersive capacity. As we know the relationship between O_3 and CO levels with weather conditions could provide information of the spatial and temporal variations shown of these chemical species. The

mentioned O_3 seasonal pattern is similar to those observed in high-latitude stations (Antarctic and sub-Antarctic regions) and is typical of remote, low NOx environments where more O_3 destruction than O_3 production occurs during summer months, resulting in a decrease in O_3 levels (Ayers et al., 1997; Parrish et al., 2016; Cristofanelli et al., 2018).

Fig. 3.

The diurnal O_3 variation is similar year-round, with nearly constant values during the first 12 hours, a slight increase of 2 to 4 ppb from midday, and a peak near 18:00 UTC. The daily cycle was similar to that measured for temperature and was opposite to that of relative humidity. Two patterns can be identified in the daily variation, according to the absolute levels, in summer and autumn (from December to May), with values from 10 to 18 ppb, and in winter and spring (from June to November), with levels from 21 to 25 ppb. As examples of the O_3 and CO hourly evolutions in summer and winter, it has been selected two periods with typical concentrations and variations (Fig. 3d-e). From 26 to 31 January 2010, O_3 had shown in these six days concentrations almost constant between 12 and 14 ppb and CO hourly values of 40 ppb. As representative of winter season, it has been stated the period from 6 to 9 July 2014 with O_3 ranging between 32 and 34 ppb and CO oscillating between 50 and 60 ppb.

Ushuaia is relatively close to the Antarctic continent, showing levels and daily and seasonal ozone patterns similar to those of Antarctic stations. However, the day-to-day variations observed on the surface remain almost constant with slight changes. Despite these levels and behaviour, O_3 chemistry does not present the two phenomena characteristic of Antarctic stations: O_3 depletion events (ODEs) (Jones et al., 2013; Mastromonaco et al., 2016) and a sudden increase of O_3 from November to January, with values close to those measured at the midwinter maximum, attributed to NOx snowpack emissions (Helming et al., 2007). The main reason for this is that Ushuaia far away from the Antarctic polar circle, out of the polar vortex, and is not surrounded by sea ice.

The CO levels show the same monthly evolution as those of O_3, with peaks in the cold months of 90 ppb and a minimum in summer of 48 ppb in January and February, with an annual oscillation of 45 ppb. The CO variability is higher than that of O_3; the monthly deviation oscillates from 2.5 to 16 ppb. This result could be associated with the influence of the weak local anthropogenic emissions, which could be mainly associated to fossil fuels burned for domestic heating. The maximum values and the highest deviations are observed in winter. The daily pattern observed for CO is similar year-round, with the highest values in the first 15 hours, a decrease at 20:00, and subsequent increase. The daily amplitude oscillates from 12 to 20 ppb based on the season. In autumn and winter, an increase between 10:00 to 14:00 is observed, which could be associated with local anthropogenic emissions, such as the use of home heating. Similar to O_3, two daily patterns can be identified, the first from December to May with values from 46 to 70 ppb and the second from June to November with values from 67 to 84 ppb.

3.3. Vertical and horizontal distribution using ozone profiles and satellite observations

The vertical behaviour of O_3 was investigated using 139 O_3 soundings launched during the measurement period (14 in autumn, 60 in spring, 28 in summer and 37 in winter) (Fig. 4). From the surface to the middle troposphere, the values range from 15 to 40 ppb. These values are lower than those obtained in remote clean environments in the Northern hemisphere under clean conditions in a remote site in the Atlantic Ocean (Andrey et al., 2014) or in the central Himalayas (Ojha et al., 2014). However, the values are similar to those recorded at a coastal Antarctic station (Jones et al., 2010).

As expected, the O_3 displays an increase with the altitude and presents a ratio of 2.8-3.9 ppb km^{-1} in the first 5000 m. The value increases from 6 to 8 km and are multiplied by a factor of 1.5-2 in a few hundred meters up to 8 km.

From 100 m to the middle troposphere, the O_3 values oscillate from 12 to 28 ppb in summer, from 16 to 34 ppb in autumn and from 26 to 42 ppb in spring and winter. From the middle troposphere, the winter and spring behaviour are reversed, with higher values in spring. These results could be associated with downward transport from upper levels. Therefore, in the middle troposphere O_3 profiles show similar seasonal behaviour to the surface O_3 observations. In the first 100 metres, the O_3 sounding values are similar to those measured on the surface, with differences lower than 3 ppb.

To investigate the spatial distribution of O_3 and CO in the Ushuaia region, observations measured with the AIRS instrument were used. A region defined by South America, the eastern Antarctic continent and the Southern Atlantic and Pacific Oceans was used to investigate the horizontal distribution of O_3 and CO. Seasonal maps were obtained from daily AIRS observations. Fig. 5 shows these seasonal maps (in summer and winter) for CO and O_3.

Fig. 4.

The horizontal distribution obtained for O_3 AIRS data indicates a clear latitudinal gradient with high levels in low latitudes, a behaviour found in all seasons. According to the AIRS observations, surface O_3 presents a weak latitudinal gradient in all seasons with the greatest variations in summer and spring, a gradient of ~3 ppb between the Antarctic Peninsula and the Ushuaia region. There were no O_3 differences around South America, i.e., between continental and marine zones. According to the results obtained from the seasonal O_3 maps, the O_3 observed in summer at Ushuaia could be representative of a wide region, with values of approximately 16-20 ppb. In autumn and winter, its spatial representativeness increases and it is very homogeneous in a wide area North and South of Ushuaia, with AIRS values of 21-23 ppb and ~30 ppb, respectively. These results indicate that surface O_3 measured at Ushuaia could be spatially representative of a wide region in the South Pacific, west of South America and the Antarctic continent.

The seasonal patterns and values of CO measured with AIRS are similar to those collected at Ushuaia. In all four seasons, differences between the continental area of South America and the surrounding oceanic regions were observed. In winter and spring, a weak latitudinal gradient in CO in latitudes higher than 55^o-60^o was observed. In summer and autumn, the studied continental area of South America shows lower values than those in the Pacific and Atlantic Oceans, with differences of approximately 10-15 ppb.

This result could be attributed to increased destruction of CO by photochemical processes in the planetary boundary layer than in the marine boundary layer. However, in winter and spring, an opposite spatial pattern is observed, with higher CO values in continental areas than in marine zones and differences of 10-15 ppb according to the AIRS measurements. In this case, these results could be associated with major CO emissions due to human activities. In addition, the lower atmosphere is more stable, so emissions are confined close to the ground. CO measurements collected at Ushuaia could be spatially representative of the continental area in the southern cone of South America due to the influence of regional emissions.

Fig. 5.

4. Discussion and conclusions

The meteorology of the Ushuaia region is governed by the arrival of airflows from the west, south of the Pacific Ocean, associated with an almost permanent low-pressure system in the western Antarctic continent. The lowest temperatures and highest relative humidity values are observed (~4 ^{o}C and 75 % respectively) in the cold months of late autumn and winter, with the lowest global solar radiation levels (less than 25 W m^{-2}), and a major probability of atmospheric stagnations (low wind speed). In these meteorological conditions, the chemical species in the lower troposphere arrives at this region by low advection processes and in well-defined layers under weak vertical mixing. Although the air masses coming from the west during all the year, the thermal and solar radiation conditions vary and affect to the photochemical processes, obtaining different O_3 and CO levels during the year.

Conversely, the highest temperatures and solar radiation (~9 ^{o}C and ~200 W m^{-2}) and lowest humidity (approximately 67 %) are observed in summer and the advection processes are more intense (the highest wind speed). The long-range transport from the west to Ushuaia is faster and the height of the MBL is greater.

The levels of surface O_3 and CO detected are similar to or lower than those observed at other high-latitude stations, such as those in Antarctica (Helmig et al., 2007; Legrand et al., 2016). Ushuaia has a mean O_3 level of 20.3±7.6 ppb and mean CO level of 71.5±45.2 ppb.

The seasonal variations in O_3 and CO at Ushuaia show a similar pattern, with a maximum in winter and a minimum in summer. The seasonal and daily patterns observed at Ushuaia with lower O_3 in summer could be associated with air transported to this site or more efficient O_3 depletion chemistry. Spring and summer O_3 levels decline due to sinks that are greater than O_3 production and transport.

The observed behaviour can be interpreted as an indicator that the MBL is dominated by net photochemical destruction of O_3, which is expected given the low or null emissions of O_3 precursors (NO_x and VOCs) in the MBL.

Although the photochemical O_3 production is supposed to be very low and the solar radiation and O_3 precursor levels are low in autumn and winter, the highest O_3 levels are observed. This could be attributed to the weakness of O_3 sinks during the cold period because of the relatively low water vapour mixing ratios and the effective O_3 transport within the MBL from the South Pacific where O_3 concentrations are higher. To corroborate these hypothesis NO_x, VOC´s and OH measurements would be necessaries in this region. Alternatively, chemical transport models could be used in future studies.

Therefore, the ozone and carbon monoxide dynamic in this region is conditioned by the absence of ozone precursors (mainly NO_X) and the long-range transport of these species through the MBL from the South Pacific Ocean. The results were corroborated by the O_3 and CO maps obtained from the satellite observations. The surface O_3 measured at Ushuaia could be representative of the low-mid troposphere, as indicated by the results obtained from O_3 profiles, and of a wide region in the South Pacific whereas CO may be representative of a continental region around the observatory and is likely affected by local emissions.

Acknowledgements.

This work was supported by the Spanish Ministerio de Economía y Competitividad (MINECO) under grant CGL2011-24891 (HELADO project). We acknowledge the NOAA Air Resources Laboratory for provision of

the HYSPLIT model. The authors thank the AEMET (Spanish State Meteorological Agency) and European Centre for Medium-Range Weather Forecasts (ECMWF) for access to the input meteorological fields.

References

Andrey, J., Cuevas, E., Parrondo, M. C., Alonso-Pérez, S., Redondas, A., Gil-Ojeda, M. 2014. Quantification of ozone reductions within the Saharan air layer through a 13-year climatologic analysis of ozone profiles. Atmos. Environ. 84, 28-34.

Ali, K., Trivedi, D. K., Sahu, S.K. 2017. Surface ozone characterization at Larsemann Hills and Maitri, Antarctica. Sci. Total Environ. DOI: 10.1016/j.scitotenv.2017.01.173.

Aumann, H. H., Chahine, M. T., Gautier, C., Goldberg, M. D., Kalnay, E., McMillin, L. M., Revercomb, H., Rosenkranz, P.W., Smith, W.L., Staelin, D.H., Strow, L.L., Susskind, J. 2003. AIRS/AMSU/HSB on the Aqua mission: Design, science objectives, data products, and processing systems. IEEE Transactions on Geoscience and Remote Sensing 41(2), 253-264.

Ayers, G.P., Granek, H.,Boers, R. 1997. Ozone in the marine boundary layer at Cape Grim: Model simulation. J. Atmos. Chem. 27(2), 179-195.

Boylan, P., Helmig, D., Oltmans, S. 2015. Ozone in the Atlantic Ocean marine boundary layer. Elementa: Science of the Anthropocene 3(1), 000045.

Cooper, O.R., Parrish, D.D., Ziemke, J., Balashov, N.V., Cupeiro, M., Galbally, I.E., Gilge, S., Horowitz, L., Jensen, N. R., Lamarque, J.-F., Naik, V., Oltmans, S.J., Schwab, J., Shindell, D.T., Thompson, A.M., Thouret, V., Wang, Y., Zbinden, R.M. 2014. Global distribution and trends of tropospheric ozone: An observation-based review. Elementa: Science of the Anthropocene 2(1), 000029.

Cristofanelli, P., Putero, D., Bonasoni, P., Busetto, M., Calzolari, F., Camporeale, G., Grigioni, P., Lupi, A., Petkov, B., Traversi, R., Udisti, R., Vitale, V. 2018. Analysis of multi-year near-surface ozone observations at the WMO/GAW "Concordia" station (75° 06' S, 123° 20' E, 3280 m asl–Antarctica). Atmos. Environ. 177, 54-63.

Dee, D.P., Uppala, S.M., Simmons, A.J., Berrisford, P., Poli, P., Kobayashi, S., Andrae, U., Balmaseda, M. A., Balsamo, G., Bauer, P., Bechtold, P., Beljaars, A.C.M., van de Berg, L., Bidlot, J., Bormann, N., Delsol, C., Dragani, R., Fuentes, M., Geer, A.J., Haimberger, L., Healy, S.B., Hersbach, H., Hólm, E.V., Isaksen, L., Kållberg, P., Köhler, M., Matricardi, M., McNally, A.P., Monge-Sanz, B.M., Morcrette, J.-J., Park, B.-K., Peubey, C., de Rosnay, P., Tavolato, C., Thépaut, J.-N., Vitart, F. 2011. The ERA-Interim reanalysis: configuration and performance of the data assimilation system. Q. J. Royal Meteorol. Soc. 137, 553–597.

Draxler, R.R., Stunder, B., Rolph, G., Taylor, A. 2009. HYSPLIT_4 User's Guide, via NOAA ARL website. NOAA Air Resources Laboratory, Silver Spring, MD, December 1997, revised January 2009. http://www.arl.noaa.gov/documents/reports/hysplit_user_ guide.pdf.

Hardacre, C., Wild, O., & Emberson, L. 2015. An evaluation of ozone dry deposition in global scale chemistry climate models. Atmos. Chem. Phys. 15(11), 6419-6436.

He, P., Bian, L., Zheng, X., Yu, J., Sun, C., Ye, P., Xie, Z. 2016. Observation of surface ozone in the marine boundary layer along a cruise through the Arctic Ocean: From offshore to remote. Atmospheric Res. 169, 191-198.

Helmig, D., Oltmans, S.J., Carlson, D., Lamarque, J.F., Jones, A., Labuschagne, C., Anlauf, K., Hayden, K. 2007. A review of surface ozone in the Polar Regions. Atmos. Environ. 41(24), 5138-5161.

IPCC. 2014. Climate Change 2013: The physical science basis. Contribution of working group I to the fifth assessment report of the intergovernmental panel on climate change.

Jones, A. E., Anderson, P. S., Wolff, E. W., Roscoe, H. K., Marshall, G. J., Richter, A., Brough, N. , Colwell, S. R. 2010. Vertical structure of Antarctic tropospheric ozone depletion events: characteristics and broader implications. Atmos. Chem. Phys. 10(16), 7775-7794.

Jones, A. E., Wolff, E.W., Brough, N., Bauguitte, S.B., Weller, R., Yela, M., Navarro-Comas, M., Ochoa, H.A., Theys, N. 2013. The spatial scale of ozone depletion events derived from an autonomous surface ozone network in coastal Antarctica. Atmos. Chem. Phys. 13(3), 1457-1467.

Lefohn, A.S., Malley, C.S., Simon, H., Wells, B., Xu, X., Zhang, L., Wang, T. 2017. Responses of human health and vegetation exposure metrics to changes in ozone concentration distributions in the European Union, United States, and China. Atmos. Environ. 152, 123-145.

Legrand, M., Preunkert, S., Jourdain, B., Galleé, H., Goutail, F., Weller, R., Savarino, J. 2009. Year-round record of surface ozone at coastal (Dumont d'Urville) and inland (Concordia) sites in East Antarctica. J. Geophys. Res.: Atmosphere 114(D20306), doi:10.1029/2008JD011667.

Legrand, M., Preunkert, S., Savarino, J., Frey, M., Kukui, A., Helmig, D., Jourdain, B., Jones, A., Weller, R., Brough, N., Gallée, H. 2016. Inter-annual variability of surface ozone at coastal (Dumont d'Urville, 2004–2014) and inland (Concordia, 2007–2014) sites in East Antarctica. Atmos. Chem. Phys. 16(12), 8053-8069.

Lin, M., Fiore, A. M., Horowitz, L. W., Cooper, O. R., Naik, V., Holloway, J., Johnson, B.J., Middlebrook, A.M., Oltmans, S.J., Pollack, I.B., Ryerson, T.B., Warner, J.X., Wiedinmyer, C., Wilson, J., Wyman, B. 2012. Transport of Asian ozone pollution into surface air over the western United States in spring. J. Geophys. Res.: Atmosphere 117(D21). DOI. 10.1029/2011JD016961.

Logan, J.A., Prather, M.J., Wofsy, S.C., McElroy, M.B. 1981. Tropospheric chemistry: A global perspective. J. Geophys. Res.: Atmosphere 86(C8), 7210-7254.

Mastromonaco, M.N., Gårdfeldt, K., Jourdain, B., Abrahamsson, K., Granfors, A., Ahnoff, M., Dommergue, A., Méjea, G., Jacobi, H.-W. 2016. Antarctic winter mercury and ozone depletion events over sea ice. Atmos. Environ. 129, 125–132.

Nara, H., Tanimoto, H., Nojiri, Y., Mukai, H., Zeng, J., Tohjima, Y., Machida, T. 2011. CO emissions from biomass burning in South-east Asia in the 2006 El Nino year: shipboard and AIRS satellite observations. Environ. Chem. 8(2), 213-223.

Nadzir, M. S. M., Ashfold, M. J., Khan, M. F., Robinson, A. D., Bolas, C., Latif, M. T., Wallis, B.M., Mead, M.I., Hamid, H.A., Harris, R.P., Ramly, Z.T.A., Lai, G.T., Liew, J.N., Ahamad, F., Uning, R., Samah, A.A., Maulud, K.N., Suparta, W., Zainudin, S.K., Wahab, M.I.A., Sahani, M., Müller, M., Yeok, F.S., Rahman, N.A., Mujahid, A., Morris, K.I. Sasso, N.D. 2018. Spatial-temporal variations in surface ozone over Ushuaia and the Antarctic region: observations from in situ measurements, satellite data, and global models. Environ Sci Pollut Res. 25(3), 2194-2210.

Ojha, N., Naja, M., Sarangi, T., Kumar, R., Bhardwaj, P., Lal, S., Venkataramani, S., Sagar, R., Kumar, A., Chandola, H.C. 2014. On the processes influencing the vertical distribution of ozone over the central Himalayas: Analysis of yearlong ozonesonde observations. Atmos. Environ. 88, 201-211.

Parrish, D.D., Galbally, I.E., Lamarque, J. F., Naik, V., Horowitz, L., Shindell, D.T., Oltmans, S. J., Derwent, R., Tanimoto, H., Labuschagne, C., Cupeiro, M. 2016. Seasonal cycles of O_3 in the marine boundary layer: Observation and model simulation comparisons. J. Geophys. Res.: Atmosphere 121(1), 538-557.

Polian, G., Lambert, G., Ardouin, B., Jegou, A. 1986. Long-range transport of continental radon in subantarctic and antarctic areas. Tellus B Chem Phys Meteorol. 38(3-4), 178-189.

Schnell, J. L., Prather, M. J., Josse, B., Naik, V., Horowitz, L. W., Cameron-Smith, P., Bergmann, D., Zeng, G., Plummer, D.A., Sudo, K., Nagashima, T., Shindell, D.T., Faluvegi, G., Strode, S.A. 2015. Use of North American and European air quality networks to evaluate global chemistry–climate modeling of surface ozone. Atmos. Chem. Phys. 15(18), 10581-10596.

Seinfeld, J.H., Pandis, S.N. 1998. Atmospheric chemistry and physics: from air pollution to climate change. Wiley Interscience, 1326 pp., New York, USA.

Simmonds, I., Keay, K., Lim, E.P. 2003. Synoptic activity in the seas around Antarctica. Mon. Weather Rev. 131(2), 272-288.

Smit, H. G. J., ASOPOS, P. 2011. Quality assurance and quality control for ozonesonde measurements in GAW. World Meteorological Organization, GAW Report, (201).

Sofen, E.D., Bowdalo, D., Evans, M.J. 2016. How to most effectively expand the global surface ozone observing network. Atmos. Chem. Phys. 16(3), 1445-1457.

Susskind, J., Barnet, C.D., Blaisdell, J.M. 2003. Retrieval of atmospheric and surface parameters from AIRS/AMSU/HSB data in the presence of clouds. IEEE Transactions on Geoscience and Remote Sensing 41, 390–409.

Stunder, B. 1996. An assessment of the quality of forecast trajectories. J. Appl. Meteorol. 35, 1319-1331.

Tarasova, O.A., Brenninkmeijer, C.A.M., Jöckel, P., Zvyagintsev, A.M., Kuznetsov, G.I. 2007. A climatology of surface ozone in the extra tropics: cluster analysis of observations and model results. Atmos. Chem. Phys. 7(24), 6099-6117.

Verma, N., Lakhani, A., Kumari, K.M. 2017. High ozone episodes at a semi-urban site in India: Photochemical generation and transport. Atmospheric Res. 197, 232-243.

Vingarzan, R. 2004. A review of surface ozone background levels and trends. Atmos. Environ. 38(21), 3431-3442.

Von Schneidemesser, E., Monks, P. S., Allan, J. D., Bruhwiler, L., Forster, P., Fowler, D., Lauer, A., Morgan, W.T., Paasonen, P., Righi, M., Sindelarova, K., Sutton, M.A. 2015. Chemistry and the linkages between air quality and climate change. Chem. Rev. 115(10), 3856-3897.

Figure captions.

Fig. 1. Mean sea level pressure maps in summer and winter (a-b) and seasonal pathways of cluster means back trajectories with 120 h run time at 500 m agl with an ending point at Ushuaia (c-f). The star on the maps marks the location of the Ushuaia observatory.

Fig. 2. Monthly evolution of temperature and relative humidity (a), wind speed and global solar radiation (b), seasonal daily variation for temperature (c) and relative humidity (d).

Fig. 3. Monthly means (standard deviation) variation of measured O_3 and CO (a) and daily seasonal variation for O_3 (b) and CO (c) measured at the Ushuaia GAW station (2010-2014), O_3 and CO hourly temporal evolutions from 26 to 31 January 2010 (d) as representative of warm season and 6 to 9 July 2014 (e) of cold season.

Fig. 4. Seasonal ozone profiles from launches at the Ushuaia GAW station.

Fig. 5. Seasonal maps of O_3 (a-d) and CO (e-h) obtained from daily AIRS observations.

Ozone and carbon monoxide at the Ushuaia GAW-WMO global station

Adame, J.A.[a,*], Cupeiro, M.[b], Yela, M.[a], Cuevas, E.[c], Carbajal, G.[d,e]

Highlights

- The levels, seasonal and daily variations of O_3 and CO at the Ushuaia GAW are analysed.
- The meteorology in this region is governed by westerly flows.
- O_3 and CO reached a maximum in winter and a minimum in summer.
- O_3 soundings and AIRS satellite observations were used.
- O_3 measurements are representative of the MBL in the South Pacific and CO of a continental local area.

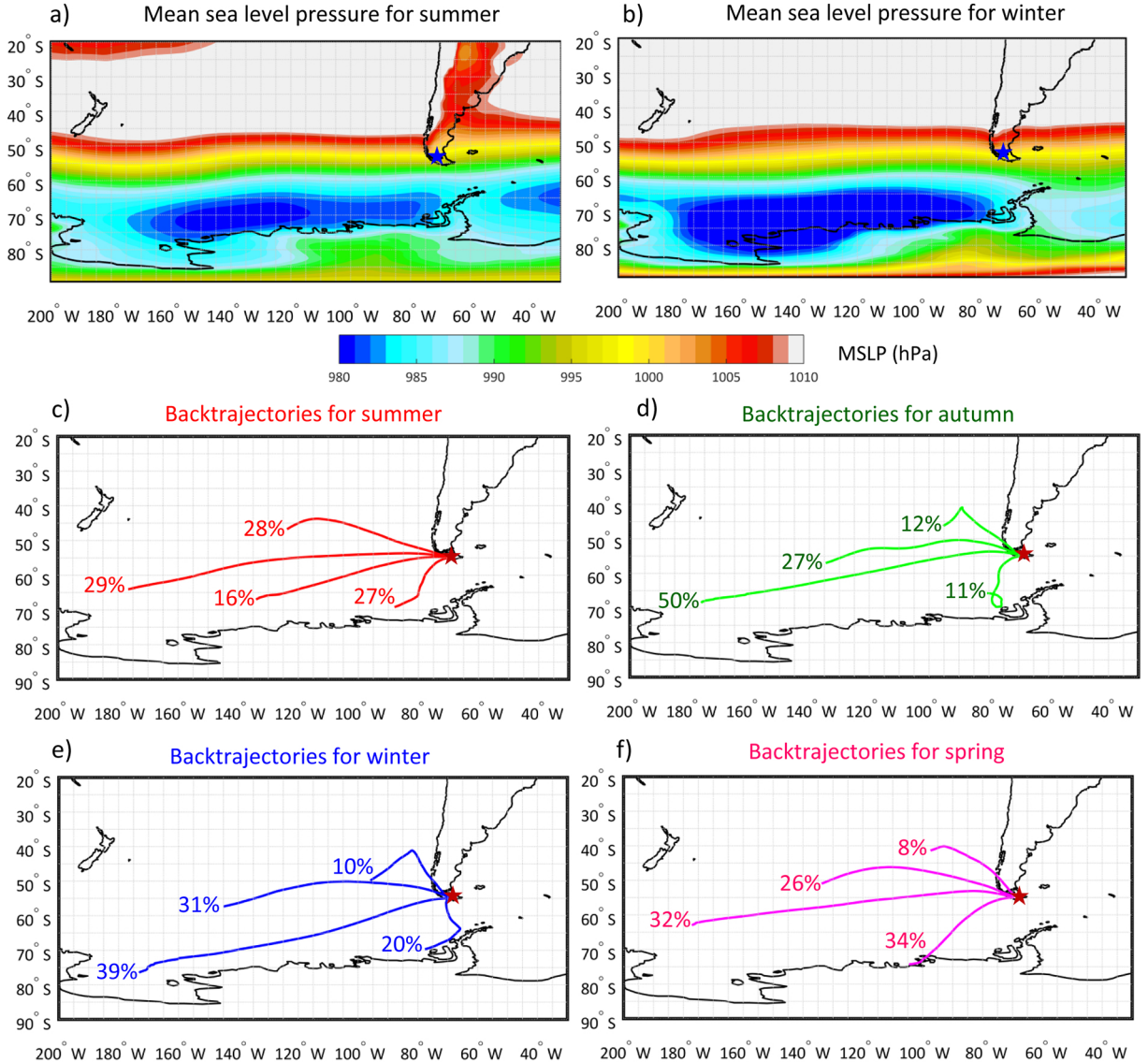
a)
Mean sea level pressure for summer
b)
Mean sea level pressure for winter
20° S
30° S
40° S
50° S
60° S
70° S
80° S
200° W 180° W 160° W 140° W 120° W 100° W 80° W 60° W 40° W
980 985 990 995 1000 1005 1010
MSLP (hPa)
c)
Backtrajectories for summer
28%
29%
16%
27%
d)
Backtrajectories for autumn
12%
27%
50%
11%
e)
Backtrajectories for winter
10%
31%
20%
39%
f)
Backtrajectories for spring
8%
26%
32%
34%

Figure 1

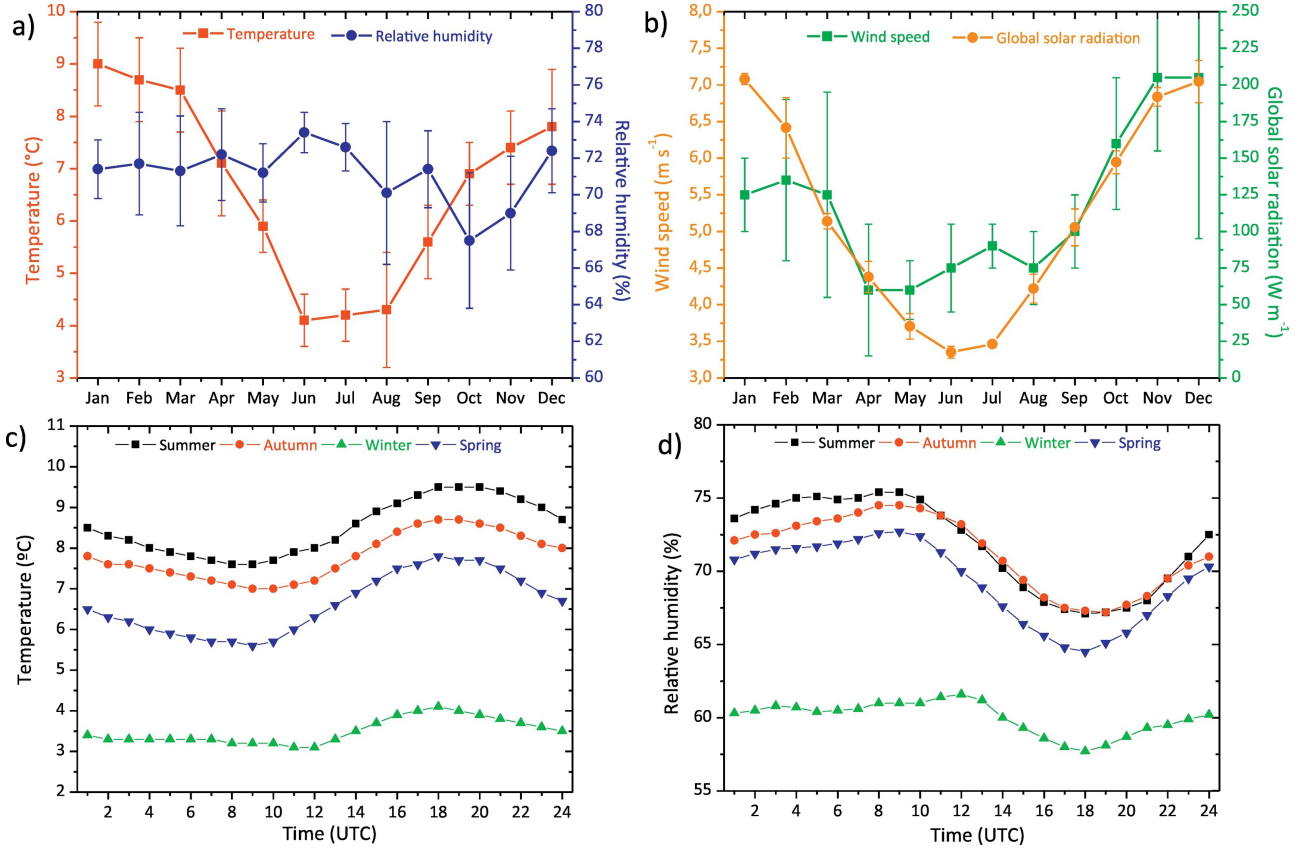
a)
Temperature
Relative humidity
Temperature (°C)
Relative humidity (%)
Jan Feb Mar Apr May Jun Jul Aug Sep Oct Nov Dec
b)
Wind speed
Global solar radiation
Wind speed (m s-1)
Global solar radiation (W m-1)
Jan Feb Mar Apr May Jun Jul Aug Sep Oct Nov Dec
c)
Summer
Autumn
Winter
Spring
Temperature (ºC)
Time (UTC)
d)
Summer
Autumn
Winter
Spring
Relative humidity (%)
Time (UTC)

Figure 2

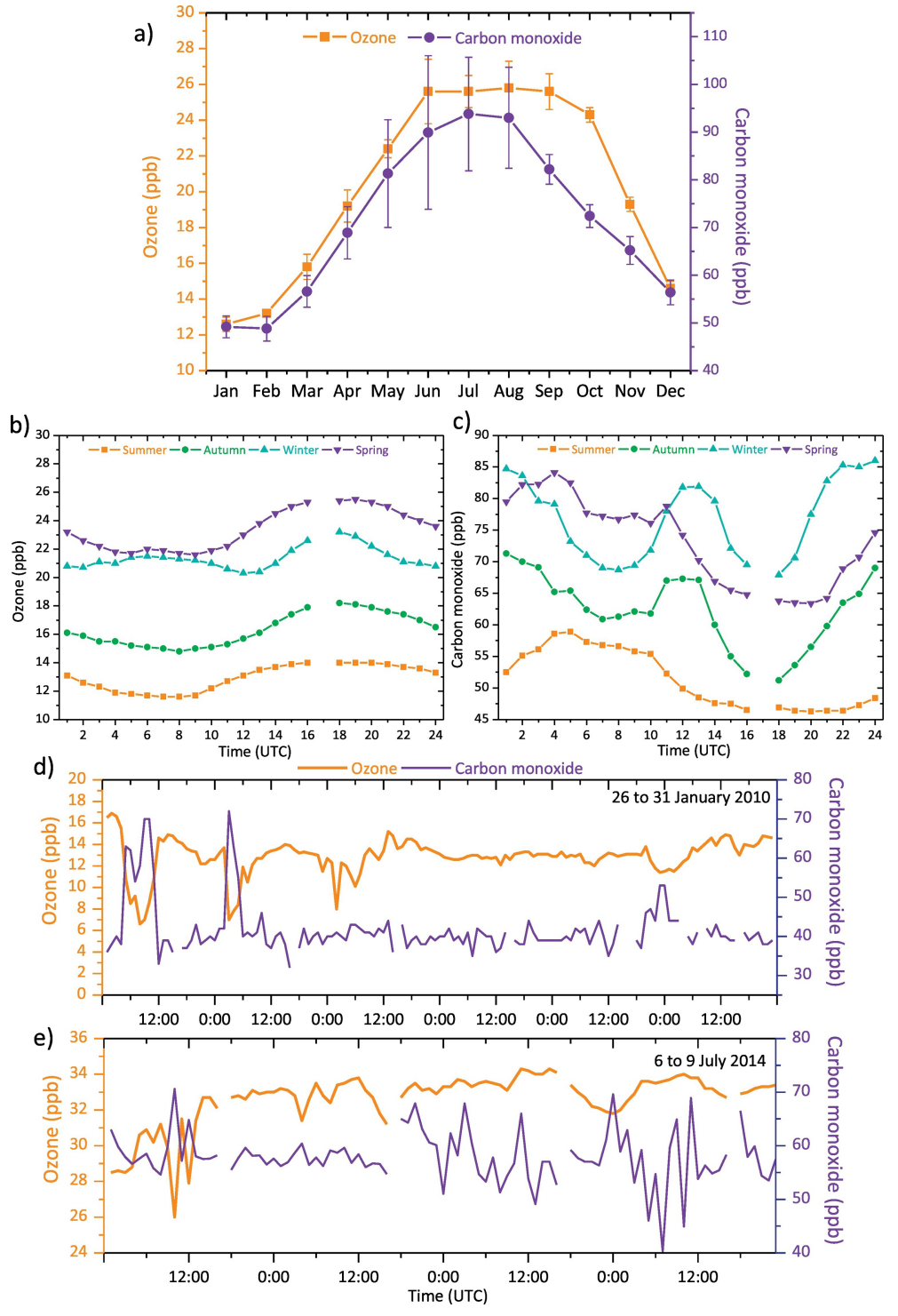
a)
Ozone
Carbon monoxide
Ozone (ppb)
Carbon monoxide (ppb)
Jan Feb Mar Apr May Jun Jul Aug Sep Oct Nov Dec
b)
Summer Autumn Winter Spring
Ozone (ppb)
Time (UTC)
c)
Summer Autumn Winter Spring
Carbon monoxide (ppb)
Time (UTC)
d)
Ozone
Carbon monoxide
26 to 31 January 2010
Ozone (ppb)
Carbon monoxide (ppb)
e)
6 to 9 July 2014
Ozone (ppb)
Carbon monoxide (ppb)
Time (UTC)

Figure 3

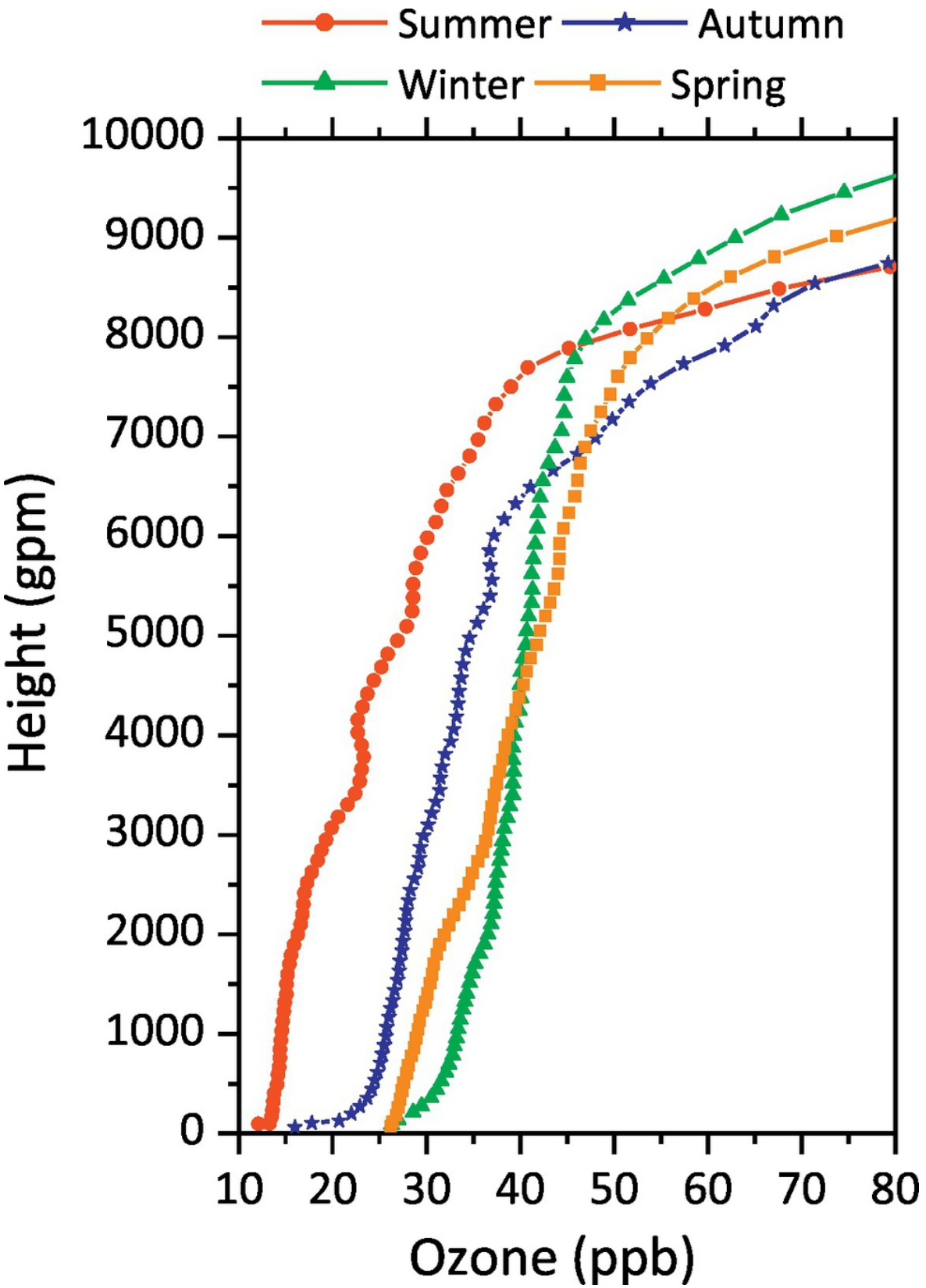
Summer
Autumn
Winter
Spring
Height (gpm)
10000
9000
8000
7000
6000
5000
4000
3000
2000
1000
0
10
20
30
40
50
60
70
80
Ozone (ppb)

Figure 4

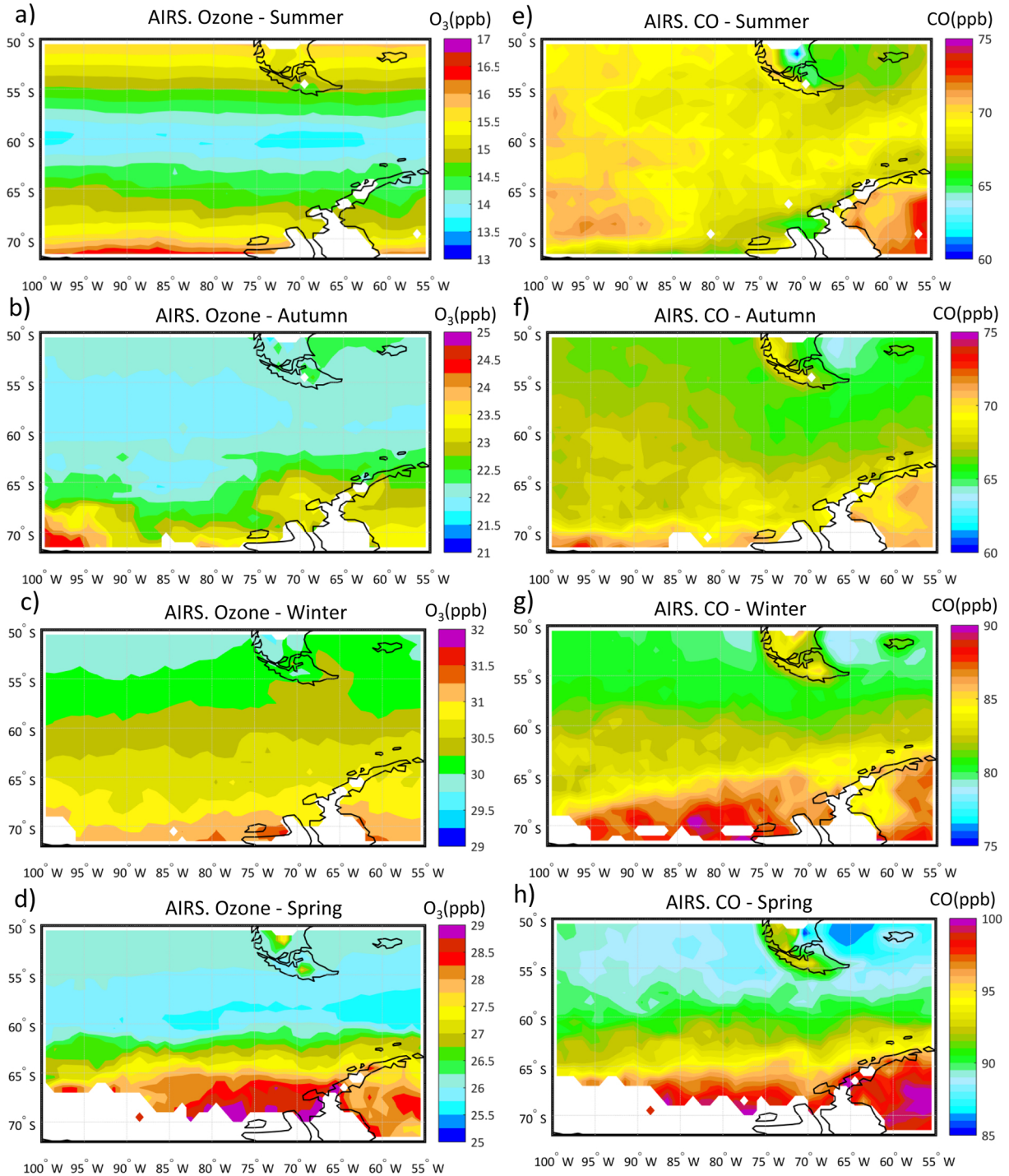
a)
AIRS. Ozone - Summer
O_3(ppb)
17
16.5
16
15.5
15
14.5
14
13.5
13
e)
AIRS. CO - Summer
CO(ppb)
75
70
65
60
b)
AIRS. Ozone - Autumn
O_3(ppb)
25
24.5
24
23.5
23
22.5
22
21.5
21
f)
AIRS. CO - Autumn
CO(ppb)
75
70
65
60
c)
AIRS. Ozone - Winter
O_3(ppb)
32
31.5
31
30.5
30
29.5
29
g)
AIRS. CO - Winter
CO(ppb)
90
85
80
75
d)
AIRS. Ozone - Spring
O_3(ppb)
29
28.5
28
27.5
27
26.5
26
25.5
25
h)
AIRS. CO - Spring
CO(ppb)
100
95
90
85
50° S
55° S
60° S
65° S
70° S
100° W 95° W 90° W 85° W 80° W 75° W 70° W 65° W 60° W 55° W

Figure 5